

Precision measurements of Hausdorff dimensions in two-dimensional quantum gravity

Jerome Barkley and Timothy Budd¹

¹ Radboud University, Nijmegen, The Netherlands.

E-mail: t.budd@science.ru.nl

Abstract. Two-dimensional quantum gravity, defined either via scaling limits of random discrete surfaces or via Liouville quantum gravity, is known to possess a geometry that is genuinely fractal with a Hausdorff dimension equal to 4. Coupling gravity to a statistical system at criticality changes the fractal properties of the geometry in a way that depends on the central charge of the critical system. Establishing the dependence of the Hausdorff dimension on this central charge c has been an important open problem in physics and mathematics in the past decades. All simulation data produced thus far has supported a formula put forward by Watabiki in the nineties. However, recent rigorous bounds on the Hausdorff dimension in Liouville quantum gravity show that Watabiki's formula cannot be correct when c approaches $-\infty$. Based on simulations of discrete surfaces encoded by random planar maps and a numerical implementation of Liouville quantum gravity, we obtain new finite-size scaling estimates of the Hausdorff dimension that are in clear contradiction with Watabiki's formula for all simulated values of $c \in (-\infty, 0)$. Instead, the most reliable data in the range $c \in [-12.5, 0)$ is in very good agreement with an alternative formula that was recently suggested by Ding and Gwynne. The estimates for $c \in (-\infty, -12.5)$ display a negative deviation from the latter formula, but the scaling is seen to be less accurate in this regime.

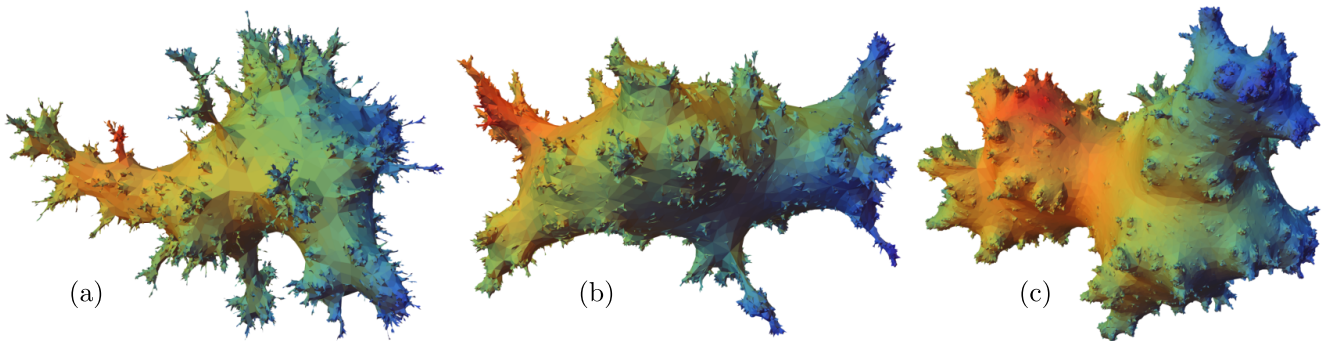


Figure 1: Three-dimensional visualizations of random surfaces sampled from three of the models under consideration: (a) spanning-tree-decorated quadrangulations, (b) bipolar-oriented triangulations, (c) Schnyder-wood-decorated triangulations. Each one consists of 2^{15} faces and is coloured (from red to blue) by increasing graph distance to a randomly sampled vertex.

1. Introduction

The emergence of scale-invariance at criticality and the universality of the corresponding critical exponents is at the center of statistical physics, underlying for instance the self-similar features of spin clusters in the Ising model at critical temperature. In a purely gravitational theory, where the configuration of a system is encoded in the spacetime geometry, criticality and self-similarity may well be realized in an ultramicroscopic limit if the theory possesses a non-trivial ultraviolet fixed point. The presence of self-similarity generally means a departure from smooth (pseudo-)Riemannian geometry and forces one to reconsider the local structure of spacetime geometry. In particular, the dimension of spacetime is no longer a clear-cut notion, but depends on the practical definitions one employs and the fractal properties of the geometry to which these definitions are sensitive. Although fractal dimensions have been studied in many quantum gravity approaches (see e.g. [1, 2, 3, 4, 5]), putting such computations on a rigorous footing is difficult. Arguably the main reason for this is the lack of explicit examples of scale-invariant statistical or quantum-mechanical ensembles of geometries, a prerequisite for the existence of exact critical exponents and fractal dimensions. Two-dimensional Euclidean quantum gravity forms an important exception in that it provides a family of well-defined such ensembles as well as a variety of rigorous mathematical tools to study them. This makes it an ideal benchmark in the computational study of fractal dimensions in quantum gravity, albeit a toy model.

Generally speaking, two-dimensional quantum gravity, the problem of making sense of the path integral over metrics on a surface, can be approached from two directions, roughly categorized as the continuum Liouville quantum gravity approach and the lattice discretization approach. In the first case, one tries to make sense of the two-dimensional metric as a Weyl-transformation $ds^2 = e^{\gamma\phi}d\hat{s}^2$ of a fixed background metric $d\hat{s}^2$, where the random field ϕ is governed by the Liouville conformal field theory with coupling $\gamma \in (0, 2]$. In the latter case one considers random triangulations (or more general random planar maps) of increasing size in the search of scale-invariant continuum limits. The famous KPZ relation [6] describing the gravitational dressing of conformal matter fields was derived in Liouville quantum gravity but shown to hold for lattice discretizations in many instances, providing a long list of exact critical exponents. These exponents, however, only indirectly witness the fractal properties of the metric.

That fractal dimensions can differ considerably from the topological dimension was first demonstrated by Ambjørn and Watabiki [7], where the volume of a geodesic ball of radius r in a random triangulation was computed to scale as r^4 (later proven rigorously [8, 9]), suggesting a Hausdorff dimension of 4 for the universality class of two-dimensional quantum gravity in the absence of matter. The self-similar random metric space of this *Brownian* universality class was later established [10, 11] in full generality as the continuum limit of random triangulations, and was recently shown [12] to agree with Liouville quantum gravity at $\gamma = \sqrt{8/3}$. While many geometric properties of the Brownian universality class are known, much less can be said about

the universality classes with $\gamma \neq \sqrt{8/3}$ which are supposed to describe scale-invariant random geometries in the presence of critical matter systems. Notably, the *spectral dimension*, a fractal dimension related to the diffusion of a Brownian particle, has been argued [13] to equal 2 for the full range of $\gamma \in (0, 2)$, which has recently been proven rigorously [14, 15]. The dependence of the Hausdorff dimension on the coupling γ , however, has been a wide open question since the nineties.

A formula for the Hausdorff dimension was put forward by Watabiki [16] based on a heuristic computation of heat kernels in Liouville quantum gravity. Written in terms of γ , which is related to the central charge c via (9), it reads

$$d_\gamma^W = 1 + \frac{\gamma^2}{4} + \sqrt{\left(1 + \frac{\gamma^2}{4}\right)^2 + \gamma^2} \quad (1)$$

and correctly predicts $d_{\sqrt{8/3}}^W = 4$ for the Brownian value and $d_\gamma^W \rightarrow 2$ in the semi-classical limit $\gamma \rightarrow 0$. However, its main support came soon after from numerical simulations of spanning-tree-decorated triangulations, a model of random triangulations in the universality class corresponding to $\gamma = \sqrt{2}$. For this model the Hausdorff dimension was estimated at $d_{\sqrt{2}} = 3.58 \pm 0.04$ [17] (and $d_{\sqrt{2}} \approx 3.55$ in [18]), in good agreement with the prediction $d_{\sqrt{2}}^W = \frac{1}{2}(3 + \sqrt{17}) \approx 3.56$. Since then all numerical estimates reported for these and other models are consistent with Watabiki's prediction [17, 19, 20, 21, 22]. The most accurate estimates are summarized in Table 1. These values, as well as measurements from Liouville quantum gravity [23], are plotted in Figure 2b.

Table 1: Previous estimates of the Hausdorff dimension.

Reference	c	γ	d_γ	d_γ^W
[21]	-20	0.867...	2.76 ± 0.07	2.6596...
[19]	-5	1.236...	3.36 ± 0.04	3.2360...
[22]	-2	$\sqrt{2}$	3.575 ± 0.003	3.5615...
[22]	1/2	$\sqrt{3}$	4.217 ± 0.006	4.2122...
[22]	4/5	$\sqrt{10/3}$	4.406 ± 0.007	4.4207...

However, recent mathematical developments in Liouville quantum gravity have shown that (1) cannot be correct for small values of γ . Ding and Goswami [24] have proven a lower bound on the Hausdorff dimension d_γ of the form

$$d_\gamma \geq 2 + C \frac{\gamma^{4/3}}{\log \gamma^{-1}} \quad (2)$$

for some unknown constant $C > 0$ and sufficiently small γ , which is seen to be incompatible with $d_\gamma^W = 2 + O(\gamma^2)$. How is it possible that an incorrect formula agrees so well with numerical data (in some cases at the three digit accuracy)? There are several conceivable explanations:

- (i) The fractal dimension we call the Hausdorff dimension in the case of triangulations measures something different compared to the one in Liouville quantum gravity.

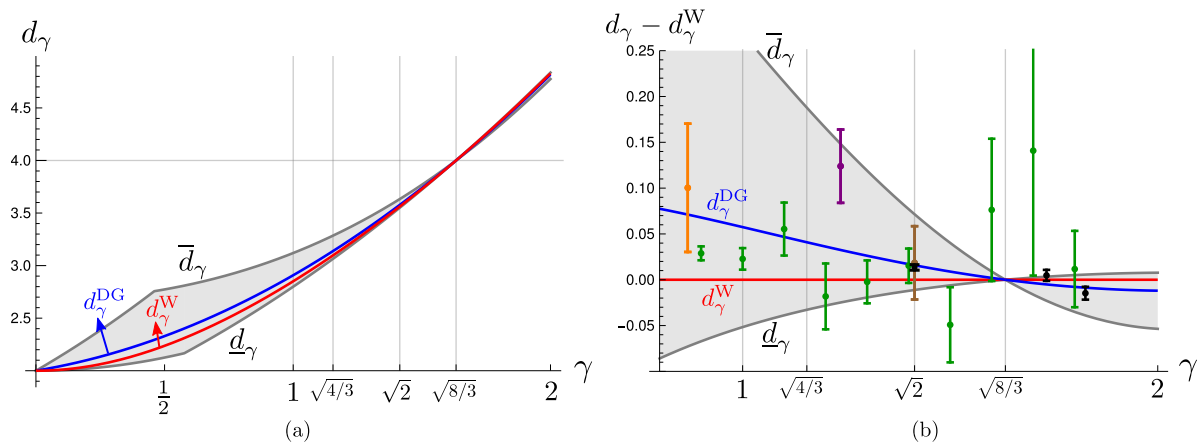


Figure 2: (a) The known bounds [28, 25, 29] on the Hausdorff dimension d_γ together with the predictions by Watabiki and Ding & Gwynne. (b) A zoomed-in version shifted by Watabiki's prediction together with numerical estimates: [17] in brown, [19] in purple, [21] in orange, [22] in black, [23] in green.

- (ii) The numerical estimate of the Hausdorff dimension in random triangulations is inaccurate.
- (iii) The actual Hausdorff dimension is not given by (1) but close enough in the tested regime to be compatible with the data.

The first option has been ruled out in a very precise sense in the works [25, 26, 27] (and references therein). In particular it is shown that Liouville Quantum Gravity possesses a unique realization as a scale-invariant random metric space for each value $\gamma \in (0, 2)$. The Hausdorff dimension d_γ of this space is a strictly increasing, continuous function of γ . Moreover, the Hausdorff dimension of various models of random triangulations, including spanning-tree-decorated triangulations and all other models considered in this paper, are shown to agree with this d_γ (with the value of γ depending on the universality class). This warrants us speaking about *the* Hausdorff dimension d_γ without specifying the precise model.

Although only the value $d_{\sqrt{8/3}} = 4$ is known, rigorous bounds have recently been derived [28, 25, 29]: $\underline{d}_\gamma \leq d_\gamma \leq \bar{d}_\gamma$ with

$$d_\gamma = \begin{cases} 2 + \frac{\gamma^2}{2} & 0 < \gamma \lesssim 0.576 \\ \frac{12 - \sqrt{6}\gamma + 3\sqrt{10}\gamma + 3\gamma^2}{4 + \sqrt{15}} & 0.576 \lesssim \gamma \leq \sqrt{8/3} \\ \frac{1}{3} \left(4 + \gamma^2 + \sqrt{16 + 2\gamma^2 + \gamma^4} \right) & \gamma \geq \sqrt{8/3}, \end{cases} \quad (3)$$

$$\bar{d}_\gamma = \begin{cases} 2 + \frac{\gamma^2}{2} + \sqrt{2}\gamma & 0 < \gamma \lesssim 0.460 \\ \frac{1}{3} \left(4 + \gamma^2 + \sqrt{16 + 2\gamma^2 + \gamma^4} \right) & 0.460 \lesssim \gamma \leq \sqrt{8/3} \\ \frac{12 - \sqrt{6}\gamma + 3\sqrt{10}\gamma + 3\gamma^2}{4 + \sqrt{15}} & \gamma \geq \sqrt{8/3}. \end{cases} \quad (4)$$

Contrary to (2), these bounds are still consistent with Watabiki's formula, see Figure 2a. Note that for $\gamma = \sqrt{2}$ the bounds imply $d_{\sqrt{2}} \in (3.550, 3.633) \subset d_{\sqrt{2}}^W + (-0.012, 0.072)$, so deviations from $d_{\sqrt{2}}^W$ will only show up in the third digit. This lends credence to explanation (iii), but does make one wonder whether it is a coincidence that a relatively simple formula like (1) precisely fits the bounds (3) and (4). However, in [25] Ding and Gwynne proposed an alternative, arguably even simpler, formula that satisfies all known bounds (2), (3) and (4),

$$d_{\gamma}^{\text{DG}} = 2 + \frac{\gamma^2}{2} + \frac{\gamma}{\sqrt{6}}. \quad (5)$$

A quick glance at Figure 2b leads one to conclude that it fits the numerical data at least as well as Watabiki's prediction does.

The goal of the current paper is to produce new numerical data to differentiate and hopefully rule out at least one of the predictions. From Figure 2 it is clear that our chances are better when looking at smaller values of γ , where d_{γ}^W and d_{γ}^{DG} differ more substantially and the window between the upper and lower bound is bigger. This is achieved by simulating a variety of random planar map models (Sections 2 and 3) as well as a discretized version of Liouville quantum gravity (Sections 4 and 5). The first study focuses on four models of random planar maps: Schnyder-wood-decorated triangulations ($\gamma = 1$), bipolar-oriented triangulations ($\gamma = \sqrt{4/3}$), spanning-tree decorated quadrangulations ($\gamma = \sqrt{2}$) and uniform quadrangulations ($\gamma = \sqrt{8/3}$). These models, the first two of which have not been studied numerically before, are particularly convenient because they can be simulated very efficiently, allowing high statistics to be obtained for surfaces with millions of vertices. Moreover, their continuum limits in relation with Liouville quantum gravity are understood in considerable detail [30, 12, 31, 32, 25]. In the second half of the paper we perform a numerical investigation of Liouville quantum gravity on a regular lattice, allowing one in principle to tune γ to any desired value.

Acknowledgments We thank the Niels Bohr Institute, University of Copenhagen, for the use of their computing facilities.

2. Four statistical models of random planar maps

To describe the models we employ terminology that is customary in the mathematical literature on random surfaces. A *planar map* is a multi-graph, i.e. an unlabeled graph with multiple edges between pairs of vertices and loops allowed, together with an embedding in the 2-sphere, such that the edges are simple and disjoint except where they meet at vertices (see e.g. Figure 3(a)). Any two planar maps that can be continuously deformed into each other are considered identical. We always take planar maps to be *rooted*, meaning that they are equipped with a distinguished oriented edge called the *root edge*. In this way we ensure that a planar map does not have any non-trivial

automorphisms, which greatly simplifies counting and random sampling. A region in the sphere delimited by d edges is called a *face of degree d* (where the edges that are incident to the face on both sides are double-counted). We denote by $\mathcal{M}_n^{(d)}$ the set of d -angulations of size n , i.e. the set of planar maps with n faces that are all of degree d . In particular $\mathcal{M}_n^{(3)}$ is the set of *triangulations* with n triangles and $\mathcal{M}_n^{(4)}$ is the set of *quadrangulations* with n squares (of genus 0 by construction). Although we will not use this, it is convenient to think of a planar map as describing a piecewise-flat surface obtained by associating to each face of degree d a regular d -gon of side length 1 and performing the gluing of the polygons according to the incidence relations of the planar map (this underlies for instance the visualizations of the large planar maps in Figure 1).

Since there are finitely many quadrangulations (or triangulations) of fixed size n , the simplest model of a random surface is to sample one such quadrangulation at random with equal probability, called the *uniform quadrangulation* of size n (see Section 2.1). To obtain different distributions one may couple the planar map to a variety of statistical systems. In the cases at hand these systems consist of decorations of a planar map by a coloring of some of its edges subject to a number of constraints. The systems are relatively simple in the sense that each decoration occurs with equal probability. The number $Z^*(\mathbf{m})$ of available decorations differs from one planar map \mathbf{m} to another, which explains the effect of the statistical system on the geometry of the random surface. In the language of statistical physics we are dealing with the *canonical partition function*

$$Z_n^* = \sum_{\mathbf{m} \in \mathcal{M}_n^{(d)}} Z^*(\mathbf{m}) = \sum_{\mathbf{m} \in \mathcal{M}_n^{(d)}} \sum_{\text{decorations of } \mathbf{m}} 1. \quad (6)$$

From a combinatorial point of view it is often hard to determine the number of decorations $Z^*(\mathbf{m})$ of a given planar map \mathbf{m} , while the total number Z_n^* of decorated planar maps is more easily accessible. Similarly, from an algorithmic point of view, it is often much easier to generate a random decorated planar map (with uniform Boltzmann weight 1) and then to forget the decoration, than it is to directly generate a random planar map with the non-trivial Boltzmann weight $Z^*(\mathbf{m})$. Below we describe four models fitting this bill and we describe in some detail the algorithms used to generate them.

In general the canonical partition function will asymptotically be of the form

$$Z_n^* \stackrel{n \rightarrow \infty}{\sim} C n^{\gamma_s - 2} \kappa^n \quad (7)$$

for some constants C , κ and γ_s . Whereas C and κ depend on the precise definition of the model, the *string susceptibility* γ_s is universal, meaning that it typically only depends on the universality class of the system. It is related via the KPZ formula [6] to the central charge c of the coupled statistical system,

$$\gamma_s = \frac{c - 1 - \sqrt{(c - 1)(c - 25)}}{12}. \quad (8)$$

In the continuum limit the geometry of a random surface coupled to a statistical system of central charge $c \in (-\infty, 1]$ is believed to be described by Liouville quantum gravity

with parameter $\gamma \in (0, 2]$ related to c and γ_s via

$$c = 25 - 6 \left(\frac{2}{\gamma} + \frac{\gamma}{2} \right)^2, \quad \gamma_s = 1 - \frac{4}{\gamma^2}. \quad (9)$$

Table 2 summarizes the relevant values for the four models.

Table 2: Critical exponents of the four models.

	γ_s	c	γ
Uniform quadrangulations (U)	$-\frac{1}{2}$	0	$\sqrt{8/3}$
Spanning-tree-decorated quadrangulations (S)	-1	-2	$\sqrt{2}$
Bipolar-oriented triangulations (B)	-2	-7	$\sqrt{4/3}$
Schnyder-wood-decorated triangulations (W)	-3	$-\frac{25}{2}$	1

2.1. Uniform quadrangulations (**U**)

As mentioned the simplest situation corresponds to quadrangulations with no decoration, i.e. to the uniform case $Z^U(\mathbf{m}) = 1$ for $\mathbf{m} \in \mathcal{M}_n^{(d)}$. The enumeration Z_n^U of (rooted) quadrangulations of size U goes back to Tutte in the sixties [33] and is given explicitly by

$$Z_n^U = \sum_{\mathbf{m} \in \mathcal{M}_n^{(4)}} 1 = 2 \frac{(2n)!}{n!(n+2)!} 3^n \stackrel{n \rightarrow \infty}{\sim} \frac{2}{\sqrt{\pi}} n^{-5/2} 12^n. \quad (10)$$

An efficient way to sample a quadrangulation of size n uniformly at random uses the Cori-Vauquelin-Schaeffer bijection [34] (see e.g. [35, Section 2.3] for a review), which provides a 2-to-1 map between quadrangulations with an additional marked vertex and certain labeled trees. Such trees can be generated easily via standard algorithms, after which the corresponding quadrangulations can be reconstructed.

2.2. Spanning-tree-decorated quadrangulations (**S**)

The first type of decorations we consider is that of spanning trees on a quadrangulation $\mathbf{m} \in \mathcal{M}_n^{(4)}$. Any quadrangulation admits a bipartition of its vertices, i.e. a black-white coloring of its vertices such that no two vertices of the same color are adjacent, that is unique if we specify that the origin of the root edge is colored white. A decoration of \mathbf{m} amounts to a choice of diagonal in each face of \mathbf{m} such that all diagonals combined form a pair of trees, one spanning the black vertices and the other spanning the white vertices (the red respectively blue tree in Figure 3b). The exact enumeration also goes back to the sixties, in this case to Mullin [36], and reads

$$Z_n^S = \sum_{\mathbf{m} \in \mathcal{M}_n^{(4)}} Z^S(\mathbf{m}) = C_n C_{n+1} \stackrel{n \rightarrow \infty}{\sim} \frac{4}{\pi} n^{-3} 16^n. \quad (11)$$

where $C_n = \frac{1}{n+1} \binom{2n}{n}$ is the n th Catalan number. The quantity $C_n C_{n+1}$ also counts the number of two-dimensional lattice walks of length $2n$ with unit steps (denoted by the cardinal directions $\{N, W, S, E\}$) starting and ending at the origin and staying in the quadrant $\mathbb{Z}_{\geq 0}^2$ (Figure 3c). This is explained by a natural encoding [36, 37] of spanning-tree-decorated quadrangulations by such lattice walks. Starting from a lattice walk the corresponding quadrangulation is constructed iteratively by starting with just the root edge with the left side designated *active* (indicated in orange in Figure 3e) and performing the operations in Figure 3d consecutively for each step of the walk.

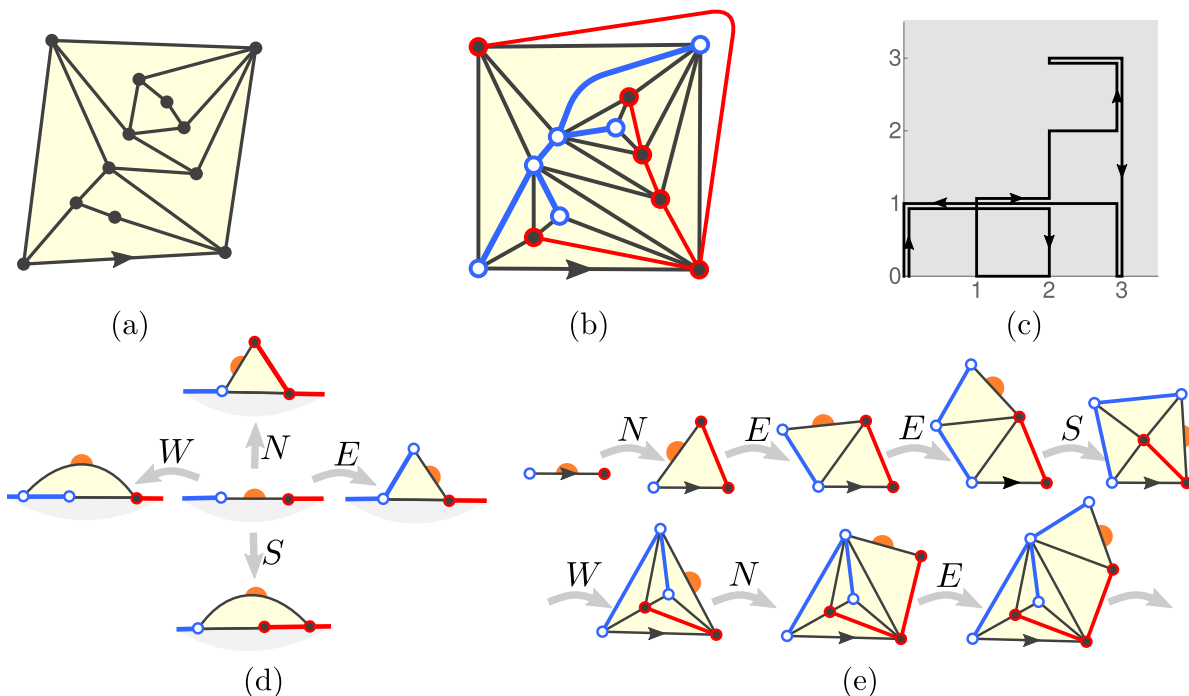


Figure 3: (a) A rooted quadrangulation in $\mathcal{M}_{10}^{(4)}$. (b) A decoration by spanning trees. (c) The corresponding $\{N, W, S, E\}$ -walk in the quadrant: N-E-E-S-W-N-E-N-E-N-W-E-S-S-S-N-W-W-W-S. (d) The schematic operations corresponding to the steps of the walk. (e) The first seven steps in the construction.

With the bijection in hand we can generate a random quadrangulation according to the partition function (11) from a uniform random $\{N, W, S, E\}$ -walk in the quadrant of length $2n$. This can be achieved efficiently by using the decomposition

$$Z_n^S = C_n C_{n+1} = \sum_{\ell=0}^n \binom{2n}{2\ell} C_\ell C_{n-\ell}, \quad (12)$$

where the summands count precisely the walks with 2ℓ horizontal steps. We may thus first sample ℓ with probability distribution $\binom{2n}{2\ell} C_\ell C_{n-\ell} / Z_n^S$ and then randomly interleave two random Dyck paths of lengths 2ℓ and $2n - 2\ell$ (one for the horizontal and one for the vertical steps).

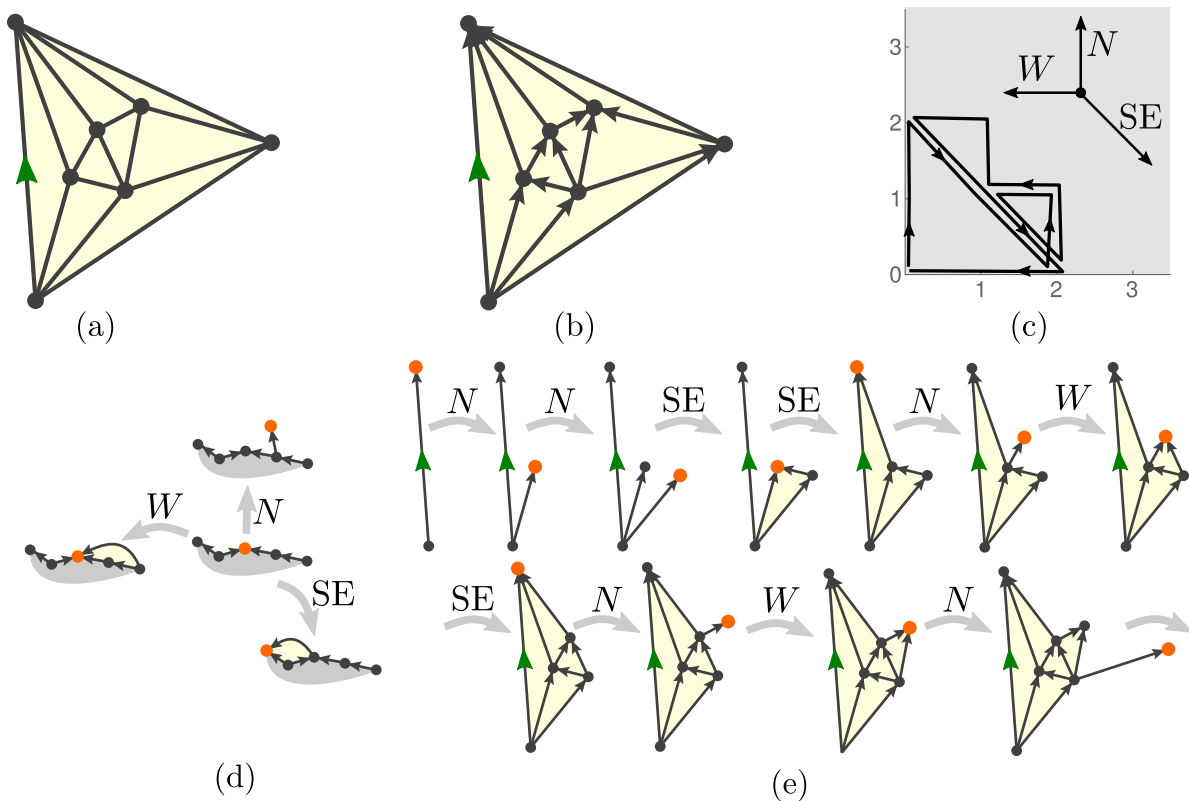


Figure 4: (a) A triangulation in $\mathcal{M}_{10}^{(3)}$ with the root in green. (b) A bipolar orientation (all edges oriented to the north). (c) The corresponding $\{N, W, SE\}$ -walk in the quadrant: N-N-SE-SE-N-W-SE-N-W-N-W-SE-SE-W-W. (d) The schematic operations corresponding to the steps of the walk. (e) The first ten steps in the construction.

2.3. Bipolar-oriented triangulations (**B**)

A bipolar orientation of a planar map \mathbf{m} is an assignment of directions to each edge of \mathbf{m} that is *acyclic*, i.e. has no directed cycles, and possesses a single *source* and *sink*, i.e. a vertex with no incoming respectively outgoing edges. Here we consider triangulations $\mathbf{m} \in \mathcal{M}_n^{(3)}$ decorated with a bipolar orientation such that the origin and end-point of the root edge are respectively the source and the sink (Figure 4b). The total number of such bipolar-oriented triangulations with $2n$ triangles was also calculated by Tutte [38, Equation (32)] (see also [39, Proposition 5.3]),

$$Z_{2n}^{\mathbf{B}} = \sum_{\mathbf{m} \in \mathcal{M}_{2n}^{(3)}} Z^{\mathbf{B}}(\mathbf{m}) = \frac{2(3n)!}{n!(n+1)!(n+2)!} \stackrel{n \rightarrow \infty}{\sim} \frac{\sqrt{3}}{\pi} n^{-4} 27^n. \quad (13)$$

Recently an encoding by lattice walks has been discovered [30] (see also [40, 41]) analogous to the spanning-tree-decorated quadrangulations. The lattice walks again start and end at the origin and stay in the first quadrant, but now consist of $3n$ steps in $\{N, W, SE\}$ (Figure 4c). To construct the bipolar-oriented triangulation from the walk, one starts with just the root edge with its endpoint designated as the *active* vertex

(orange in Figure 4e) and applies the operations in Figure 4d according to the steps of the walk (except the very last).

To generate a $\{N, W, SE\}$ -walk efficiently, we make use of the fact that the number of walks from (x, y) to $(0, 0)$ of length $3m + x + 2y$ is known [42, Proposition 9] to be

$$\frac{(x+1)(y+1)(x+y+2)(3m+x+2y)!}{m!(m+y+1)!(m+x+y+2)!}. \quad (14)$$

From this it follows that if a random $\{N, W, SE\}$ -walk of length $3n$ is at (x, y) after $3n - k$ steps, then the next step will be N , W or SE with probabilities

$$\begin{aligned} N: & \frac{(y+2)(x+y+3)(k-x-2y)}{3k(y+1)(x+y+2)}, & W: & \frac{x(x+y+1)(k+2x+y+6)}{3k(x+1)(x+y+2)}, \\ SE: & \frac{y(x+2)(k-x+y+3)}{3k(x+1)(y+1)}. \end{aligned} \quad (15)$$

This allows one to sample the walk iteratively in quasi-linear time.

2.4. Schnyder-wood-decorated triangulations (\mathbf{W})

Let $\mathbf{m} \in \mathcal{M}_{2n}^{(3)}$ be a *simple* triangulation, meaning that it contains no double edges or loops (Figure 5a). Color the origin of the root edge, the endpoint of the root edge, and the remaining vertex incident to the triangle on the right of the root edge red, green, and blue respectively. The edges that are incident to at least one uncolored vertex are called *inner* edges. A *Schnyder wood* (also known as a *realizer*) [43] on \mathbf{m} is a coloring in red, green, and blue and an orientation of all inner edges (Figure 5c) satisfying the following properties:

- Each uncolored vertex has precisely one outgoing edge of each color. Moreover, the incoming and outgoing edges of the various colors are ordered around the vertex as in Figure 5b.
- The inner edges incident to a colored vertex are all incoming and of the same color as the vertex.

According to [44, Corollary 19] the number of Schnyder-wood-decorated triangulations with $2n$ triangles is

$$Z_{2n}^{\mathbf{W}} = \sum_{\mathbf{m} \in \mathcal{M}_{2n}^{(3)}} Z^{\mathbf{W}}(\mathbf{m}) = C_{n-1}C_{n+1} - C_n^2 \stackrel{n \rightarrow \infty}{\sim} \frac{3}{2\pi} n^{-5} 16^n. \quad (16)$$

Also for this model an encoding in terms of lattice walks in the quadrant is known [44, 45, 46, 32], in this case consisting of $2n - 2$ steps in $\{E, W, NW, SE\}$ starting and ending at the origin (Figure 5d). The way the encoding works is a bit different compared to the spanning-tree-decorated quadrangulations and bipolar-oriented triangulations. First of all one represents the $\{E, W, NW, SE\}$ -walk as a *double Dyck path* of length $2n - 2$, i.e. a pair of walks in the quadrant from the origin to $(2n - 2, 0)$ with steps in

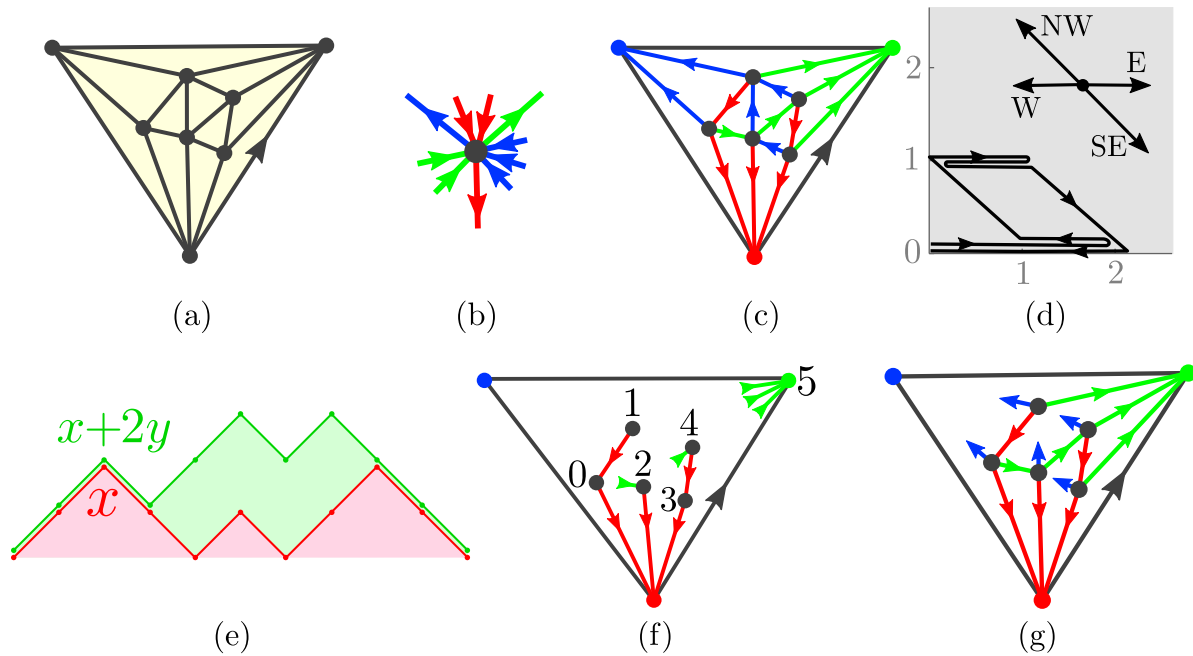


Figure 5: (a) A simple triangulation in $\mathcal{M}_{12}^{(3)}$. (b) The condition on the ordering of edges around inner vertices. (c) A Schnyder wood. (d) The corresponding $\{E, W, NW, SE\}$ -walk of length 10: E-E-W-NW-E-W-E-SE-W-W. (e) The corresponding double Dyck path. (f) The red tree together with the endpoints of the green edges as encoded by the double Dyck path. (g) As soon as the red and green edges are known, the blue edges (one for each uncolored vertex) are determined.

$\{NE, SE\}$ such that the first path does not go below the second (Figure 5e). This is achieved by plotting the graph of x and $x+2y$ where (x, y) ranges over the coordinates of the $\{E, W, NW, SE\}$ -walk. To construct the triangulation we start with a single triangle with colored vertices and attach a red tree to the red vertex as encoded by the lower Dyck path in the usual fashion (“apply glue to the bottom of the Dyck path and squash horizontally”). We then label the uncolored vertices of the red tree from 0 to $n-2$ in the order in which they are encountered when tracing the contour of the tree in clockwise direction, and assign label $n-1$ to the green vertex (Figure 5f). The upper Dyck path is then used to determine the position of the endpoints of the green edges: for each SE -step that is preceded by a total of k NE -steps we add an endpoint to the vertex with label k . Since a single green edge has to start at each uncolored vertex (and end at the indicated positions), it is easy to see that there is a unique way to draw them while satisfying the condition in Figure 5b. As soon as the red and green edges are drawn (Figure 5g) the blue edges are also uniquely determined by this condition.

As in the case of the bipolar-oriented triangulations, there is an efficient method to generate random $\{E, W, NW, SE\}$ -walks of length $2n-2$. The total number of such

walks of length $2m + x$ starting at (x, y) and ending at the origin is [39, Proposition 11]

$$\frac{(x+1)(y+1)(x+y+2)(x+2y+3)}{(2m+x+1)(2m+x+2)(2m+x+3)^2} \binom{2m+x+3}{m-y} \binom{2m+x+3}{m+1}. \quad (17)$$

It follows that if a random $\{E, W, NW, SE\}$ -walk of length $2n - 2$ is at (x, y) after $2n - 2 - k$ steps that the next step will be E, W, NW, SE with probabilities

$$\begin{aligned} E: & \frac{(x+2)(k-x+2)(x+y+3)(x+2y+4)(k-x-2y)}{4k(k+2)(x+1)(x+y+2)(x+2y+3)}, \\ W: & \frac{x(k+x+4)(x+y+1)(x+2y+2)(k+x+2y+6)}{4k(k+2)(x+1)(x+y+2)(x+2y+3)}, \\ NW: & \frac{x(y+2)(k+x+4)(x+2y+4)(k-x-2y)}{4k(k+2)(x+1)(y+1)(x+2y+3)}, \\ SE: & \frac{(x+2)y(k-x+2)(x+2y+2)(k+x+2y+6)}{4k(k+2)(x+1)(y+1)(x+2y+3)}. \end{aligned}$$

3. Finite-size scaling analysis of (dual) graph distances

As discussed in the introduction, the Hausdorff dimension d_γ for $\gamma = \sqrt{8/3}, \sqrt{2}, \sqrt{4/3}, 1$ agrees with the growth exponent of the volume $|\text{Ball}_r(\mathbf{m}_n)|$ of the ball of radius r , i.e. the number of vertices that have graph distance at most r from a random initial vertex, in a random map \mathbf{m}_n of size n sampled from model (U), (S), (B), (W) respectively,‡

$$\frac{\log |\text{Ball}_r(\mathbf{m}_n)|}{\log r} \xrightarrow[n \gg r]{n, r \rightarrow \infty} d_\gamma. \quad (18)$$

Since we cannot attain the limit $n, r \rightarrow \infty$ in simulations, we employ the finite-size scaling method to estimate the exponents. To this end, we need to make a few additional, but reasonable, assumptions. Let R_n be the graph distance between two uniformly sampled vertices in a random planar map of size n (sampled from one of the models). For integer r we set $\rho_n^{(*)}(r) = \mathbb{P}(R_n = r)$ to be the probability that this distance is r , and we extend $\rho_n^{(*)}$ to a continuous function $\rho_n^{(*)} : (0, \infty) \rightarrow [0, \infty)$ by interpolation. We assume that for any $x > 0$

$$\lim_{n \rightarrow \infty} n^{1/d_\gamma} \rho_n^{(*)}(x n^{1/d_\gamma}) = \rho^{(*)}(x) \quad (19)$$

for a continuous probability distribution $\rho^{(*)}$ on $(0, \infty)$ that depends only on the model $(*)$. This is slightly stronger than the requirement that $R_n/n^{1/d_\gamma}$ converges in distribution as $n \rightarrow \infty$. As we will see shortly (19) is well supported by our data and known to be correct for uniform quadrangulations (with an explicit limit [47]).§ Note, however, that it does not quite imply (18), nor is it implied by (18).

‡ In probabilistic terms, the limit can be understood as a limit in distribution as $n \rightarrow \infty$ followed by an almost sure limit as $n \rightarrow \infty$ [25, Theorem 1.6].

§ In the case of spanning-tree decorated quadrangulations [31, Theorem 1.4] comes close by identifying the scaling of the diameter of \mathbf{m}_n with growing n .

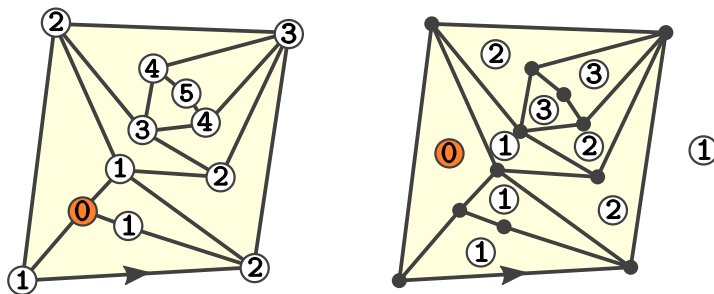


Figure 6: The graph distance (left) and dual graph distance (right) in a quadrangulation.

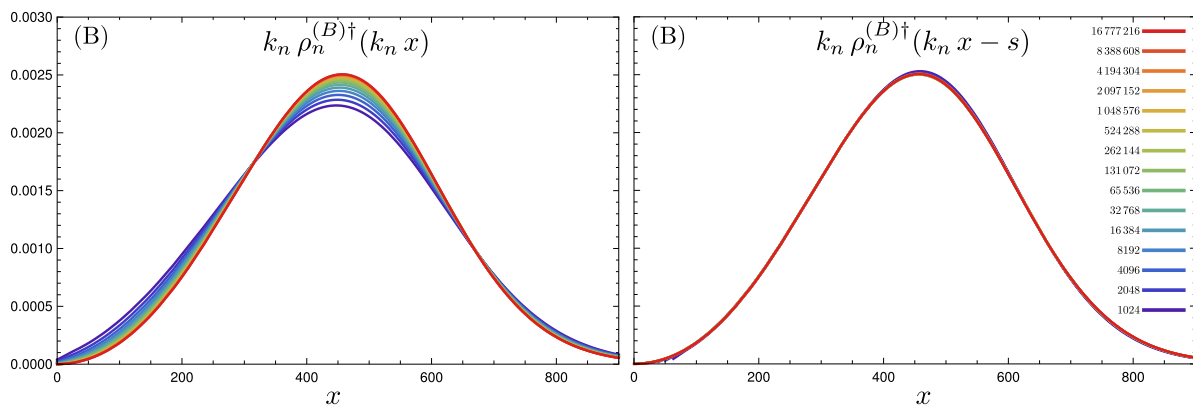


Figure 7: Finite-size scaling for the dual graph distance in bipolar-oriented triangulations without shift (left) and with shift $s = 2.941$ (right). The effect in the case of graph distance is less pronounced.

We estimate $\rho_n^{(*)}$ with high accuracy for each model $(*)$ and sizes n ranging from 2^8 up to 2^{24} (≈ 17 million) by sampling a large ensemble of random planar maps (10^7 for small n and 10^5 for $n \geq 2^{19}$). In each random planar map we pick a single uniform random vertex and determine the graph distance to all other vertices in the map (Figure 6). All these distances for the planar maps in an ensemble are included in a histogram, which upon normalization and interpolation provides our estimate of $\rho_n^{(*)}$. It turns out to be convenient to supplement the analysis with another distribution $\rho_n^{(*)\dagger}$ that relies on a different notion of distance: the *dual* graph distance between two uniformly sampled faces in the planar map (right side of Figure 6). It is estimated in an analogous way, this time picking a uniform random face and determining the distances to all other faces.

To test the convergence (19) we choose optimal parameters k_n to “collapse” the functions $x \mapsto k_n^{-1} \rho_n^{(*)}(k_n^{-1}x)$. To be precise, we denote by $n_0 = 2^{24}$ the largest system size and take $\rho_{n_0}^{(*)}$ as the reference distribution. Then for each $n \leq n_0$, k_n is obtained by fitting $x \mapsto k_n^{-1} \rho_n^{(*)}(k_n^{-1}x)$ to $x \mapsto \rho_{n_0}^{(*)}(x)$, such that $k_n > 1$ for $n < n_0$ and $k_{n_0} = 1$ by construction. In the fit we choose to only take into account the portion of the histogram for which $\rho_n^{(*)}(r) \geq \frac{1}{5} \max_{r'} \rho_n^{(*)}(r')$, thus avoiding the tails of the distribution that are more prone to discretization effects.

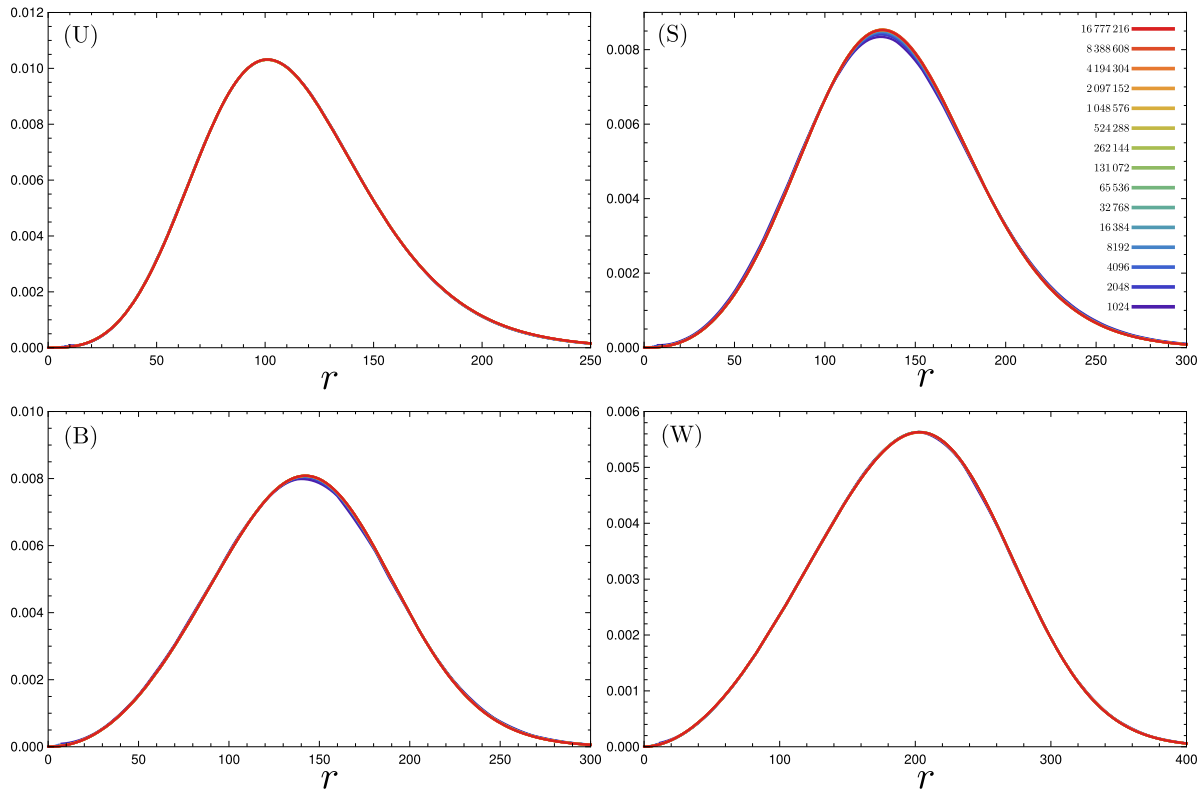


Figure 8: Finite-size scaling of the graph distance in the four models with sizes ranging from $2^{10} = 1024$ to $2^{24} = 16\,777\,216$ and shifts as listed in the table.

The collapse of $\rho_n^{(B)\dagger}$ in the case of dual graph distance on bipolar-oriented triangulations is shown in the left plot of Figure 7. A qualitative convergence is certainly observed, but one has to go to quite large sizes for the curves to become indistinguishable. A common technique [48, 17, 49] to improve the collapse is by introducing a *shift* $\rho_n^{(*)}(r) \rightarrow \rho_n^{(*)}(r - s)$ in the histograms before performing the scaling, where $s \in \mathbb{R}$ is independent of n . For any fixed s , the convergence $n^{1/d_\gamma} \rho_n^{(*)}(xn^{1/d_\gamma} - s) \xrightarrow{n \rightarrow \infty} \rho^{(*)}(x)$ is of course equivalent to our scaling ansatz (19). One may think of this shift as absorbing a subleading correction in (19) or, if you like, accounting for the freedom we have in the discrete setting to assign distance s instead of 0 to the initial vertex/face. The optimal shift s is determined by fitting $x \mapsto k_n^{-1} \rho_n^{(*)}(k_n^{-1}(x + s_n) - s_n)$ to $x \mapsto \rho_{n_0}^{(*)}(x)$ for each n and taking s to be a (weighted) average of the values s_n . This way we fix s once and for all to the values in Table 3.

Table 3: Optimal shift parameters

Model	Graph distance	Dual graph distance
(U)	$s = 0.940$	$s = 4.608$
(S)	$s = 0.557$	$s = 3.019$
(B)	$s = 0.359$	$s = 2.941$
(W)	$s = 0.439$	$s = 2.629$

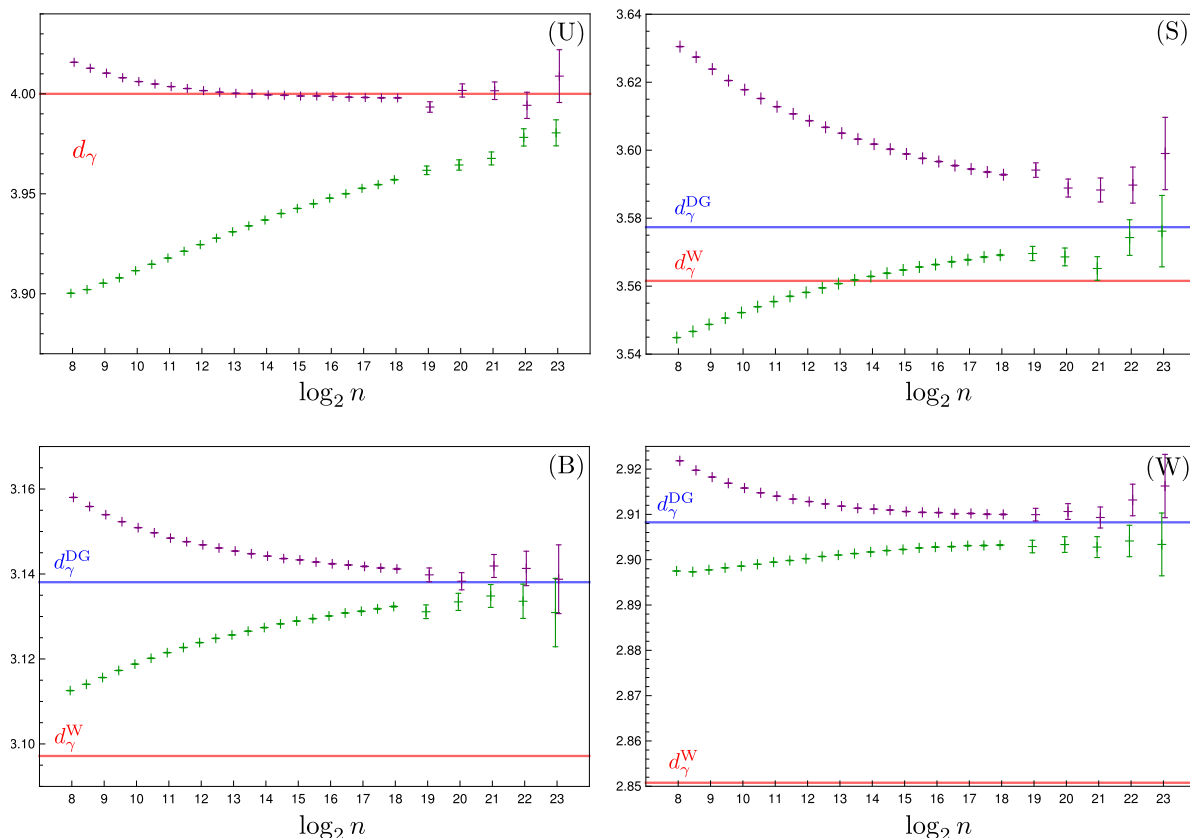


Figure 9: Plots of $\frac{\log(n_0/n)}{\log(k_n/k_{n_0})}$ with statistical error bars for all four models, showing both graph distance (purple) and dual graph distance (green) measurements. Watabiki's and Ding-Gwynne's predictions are indicated by horizontal lines.

With s fixed we determine the optimal scaling k_n yet again by fitting $x \mapsto k_n^{-1} \rho_n^{(*)}(k_n^{-1}(x+s) - s)$ to $x \mapsto \rho_{n_0}^{(*)}(x)$. The result in the case of $\rho_n^{(B)\dagger}$ is shown in the right plot of Figure 7. This time all curves for $n \gtrsim 2^{13}$ become indistinguishable at the resolution of the plot. The finite-size scaling of the graph distance including the shift is shown in Figure 8 for all four models. The very accurate scaling lends support to the existence of a continuous probability distribution $\rho^{(*)}$ in the limit (19).

If (19) is satisfied then

$$k_n \stackrel{n \rightarrow \infty}{\sim} c (n/n_0)^{-1/d_\gamma} \quad (20)$$

for some constant $c \approx 1$. To get a first idea of the rate of convergence to the asymptotics (20), we plot in Figure 9 the logarithmic ratios

$$\frac{\log(n_0/n)}{\log(k_n/k_{n_0})} \quad (21)$$

with statistical error bars for the four models using both the graph distance (purple) and its dual (green). The advantage of considering the different distance measurements becomes clear upon inspecting these plots: the deviations from the scaling relation (20) appear with different sign, allowing one in principle to estimate the exponent d_γ by eye

at the point where the two curves converge. It is also immediately clear that the data is incompatible with d_γ^W in the case of bipolar-oriented and Schnyder-wood-decorated triangulations, and is much closer to d_γ^{DG} .

To accurately estimate d_γ , we make an ansatz for the leading-order correction to (20) of the form

$$k_n \approx \left(\frac{n}{n_0}\right)^{-\frac{1}{d}} \left(a + b \left(\frac{n}{n_0}\right)^{-\delta}\right), \quad (22)$$

where a is close to 1, b is small and $\delta > 0$. The best fits are given in Table 4, including the statistical errors on d . Finally, combining the data from both distance measures yields the estimates for the Hausdorff dimension recorded in Table 5 and plotted in Figure 11.

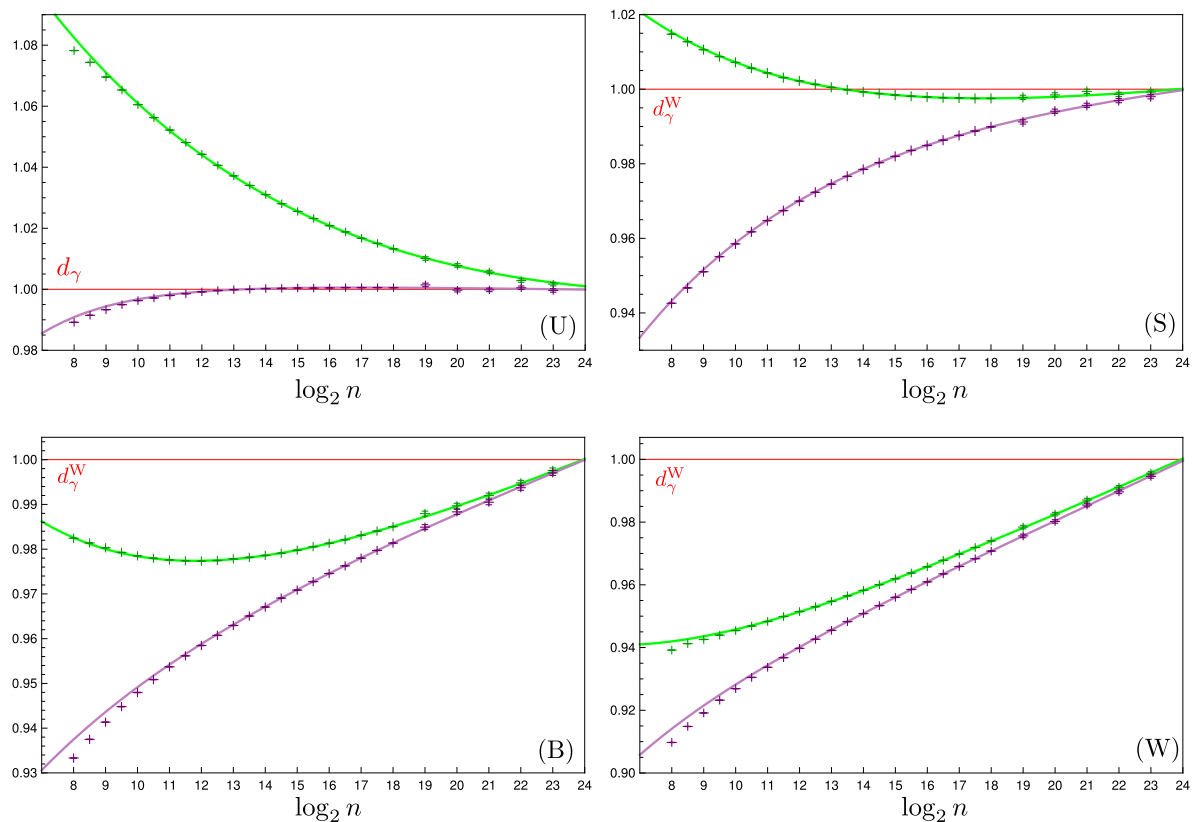


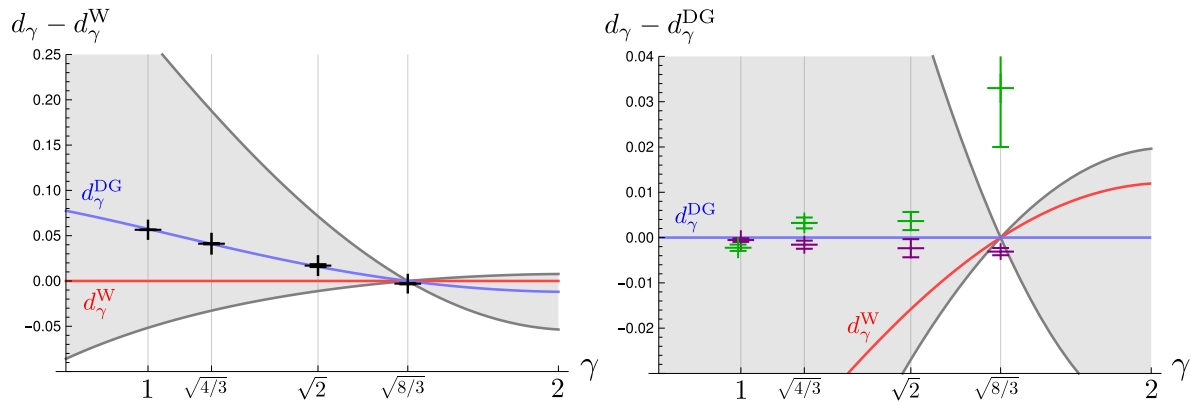
Figure 10: Plots of $k_n(n/n_0)^{1/d_\gamma^W}$ with the scaling parameters k_n established via finite-size scaling of the graph distance (purple) and dual graph distance (green). The solid curves correspond to best fits of the ansatz (22).

Table 4: Parameters of the best fit of the data to the ansatz (22).

Model	d	δ	a	b
(U)	3.9969 ± 0.0013	0.57	0.99992	-0.000020
(U)†	4.037 ± 0.024	0.16	0.9795	0.0206
(S)	3.575 ± 0.006	0.26	1.0025	-0.00275
(S)†	3.581 ± 0.004	0.26	0.9982	0.00190
(B)	3.136 ± 0.002	0.29	1.00081	-0.00084
(B)†	3.141 ± 0.003	0.27	0.9984	0.0018
(W)	2.9077 ± 0.0010	0.41	0.99968	-0.00014
(W)†	2.906 ± 0.002	0.33	0.99985	0.00038

Table 5: Hausdorff dimension estimates for the four planar map models.

Model	γ	d_γ	d_γ^W	d_γ^{DG}
(U)	$\sqrt{8/3}$	3.9970 ± 0.0013	4.0000	4.0000
(S)	$\sqrt{2}$	3.5791 ± 0.0033	3.5616	3.5774
(B)	$\sqrt{4/3}$	3.1375 ± 0.0017	3.0972	3.1381
(W)	1	2.9074 ± 0.0009	2.8508	2.9083


Figure 11: The plot on the left shows the estimates of d_γ in comparison to d_γ^W in the same scale as Figure 2b. The right plot shows the individual estimates of d_γ using the graph distance (purple) and dual graph distance (green) in comparison with d_γ^{DG} .

4. Hausdorff dimensions in Liouville quantum gravity

Simulations of the four planar maps models have provided accurate estimates of the Hausdorff dimension d_γ for $\gamma = 1, \sqrt{4/3}, \sqrt{2}, \sqrt{8/3}$. In principle one can extend this method by exploring new discrete models that live in other universality classes. However, finding such models that allow for efficient simulation is a non-trivial task^{||}. An alternative route is to start from the continuum description of Liouville quantum gravity.

Formally one thinks of the random two-dimensional metric as a Weyl-transformation $g_{ab} = e^{\gamma\phi}\hat{g}_{ab}$ of a fixed background metric \hat{g}_{ab} on the surface. The field

^{||} The *mated-CRT maps* of [50] are a good candidate for arbitrary $\gamma \in (0, 2)$.

ϕ is sampled with probability proportional to $e^{-S_L[\phi]}$ with the Liouville action given by [6, 51, 52]

$$S_L[\phi] = \frac{1}{4\pi} \int d^2x \sqrt{\hat{g}(x)} (\hat{g}^{ab} \partial_a \phi \partial_b \phi + Q \hat{R} \phi + 4\pi \lambda e^{\gamma \phi}), \quad (23)$$

where \hat{R} is the scalar curvature of \hat{g}_{ab} , λ the *cosmological constant*, and $Q = 2/\gamma + \gamma/2$. Since we are only interested in the local properties of the metric g_{ab} we may as well choose $\lambda = 0$ and fix $\hat{g}_{ab} = \delta_{ab}$ to the standard Euclidean metric on the unit torus (using periodic coordinates $x \in \mathbb{R}^2/\mathbb{Z}^2$). In this case the action (23) becomes that of a scalar free field,

$$S_L[\phi] = S_{\text{GFF}}[\phi] = \frac{1}{4\pi} \int_{\mathbb{R}^2/\mathbb{Z}^2} d^2x \nabla \phi \cdot \nabla \phi. \quad (24)$$

The random field ϕ sampled with (suitably regularized) probability $e^{-S_{\text{GFF}}[\phi]}$ is called the *Gaussian free field* in the mathematical literature [53]. The pointwise values of ϕ are not well-defined, but the field can be rigorously understood as a random generalized function (or distribution) living in an appropriate Sobolev space. This implies that the identification $g_{ab} = e^{\gamma \phi(x)} \hat{g}_{ab}$ cannot make literal sense as a random Riemannian metric without choosing a regularization scheme. At the level of the volume form $\sqrt{g} d^2x = e^{\gamma \phi(x)} d^2x$ this can be achieved by imposing an ultraviolet cutoff ϵ on ϕ , e.g. by setting $\phi_\epsilon(x)$ to be the average of ϕ over a circle of radius ϵ centered at x , and considering the limit

$$\lim_{\epsilon \rightarrow 0} \epsilon^{\gamma^2/2} e^{\gamma \phi_\epsilon(x)} d^2x \quad (25)$$

viewed as a random measure, called the γ -Liouville measure [54].

Determining a regularization scheme of $g_{ab} = e^{\gamma \phi(x)} \hat{g}_{ab}$ that gives rise to well-defined geodesic distances $d(x, y)$ between pairs of points is more challenging. The intuitive reason for this is that the distance between two points is realized by a curve that generically has a fractal structure (in the Euclidean background metric), meaning that its length will be quite sensitive to the way the ultraviolet cutoff is imposed. Nevertheless, there has been much progress in recent years, resulting in at least two different approaches.

4.1. Liouville graph distance

The *Liouville graph distance* $D_{\gamma, \delta}(x, y)$ between two points is defined as the fewest number of Euclidean disks of arbitrary radius, but volume at most δ as measured by the γ -Liouville measure, needed to cover a path connecting x and y [24, 55, 25]. This definition should be viewed as the analogue of the (dual) graph distance in a random planar map of size $n \approx \delta^{-1}$, where the distance is the fewest number of faces (which all have equal volume ≈ 1) one has to traverse to get from one vertex to another. It has been shown rigorously [25, Theorem 1.4] that $D_{\gamma, \delta}(x, y)$ for fixed x and y is of order δ^{-1/d_γ} , i.e.

$$\lim_{\delta \rightarrow 0} \frac{\log D_{\gamma, \delta}(x, y)}{\log \delta} = -\frac{1}{d_\gamma}. \quad (26)$$

This provides one avenue to measure d_γ numerically, as was done by Ambjørn and the second author in [23]. There a discrete γ -Liouville measure was constructed by exponentiating a discrete Gaussian free field (see Section 4.3 below) on a $w \times w$ square lattice with periodic boundary conditions. Instead of finding paths of disks of volume δ connecting pairs of points, distances were obtained from a Riemannian metric with local density constructed from averaging the γ -Liouville measure over such disks of volume δ , for which one expects similar behaviour. Estimates on d_γ obtained in [23] are shown in green in Figure 2b.

4.2. Liouville first passage percolation

Following [56, 24, 55, 25, 26], the *Liouville first passage percolation* distance $D_{\xi,\epsilon}(x, y)$ between two points x and y is given for $\xi > 0$ in terms of the regularized Gaussian free field ϕ_ϵ by

$$D_{\xi,\epsilon}(x, y) = \inf_{\Gamma:x \rightarrow y} \int_0^1 e^{\xi \phi_\epsilon(\Gamma(t))} |\Gamma'(t)| dt, \quad (27)$$

where the infimum is over piecewise differentiable paths Γ with $\Gamma(0) = x$ and $\Gamma(1) = y$.

In the hope to construct a metric for γ -Liouville quantum gravity one should *not* take $\xi = \gamma/2$, which would arise from naively regularizing the Riemannian metric as $e^{\gamma \phi_\epsilon(x)} \hat{g}_{ab}$. Assuming the existence of a Hausdorff dimension d_γ , one would like an overall scaling of the volume (as measured by the γ -Liouville measure) by a factor C to amount to a scaling of the geodesic distances by C^{1/d_γ} . The former is achieved by a constant shift $\phi(x) \rightarrow \phi(x) + \frac{1}{\gamma} \log C$ in (25), leading to an overall scaling of (27) by $C^{\xi/\gamma}$, hence suggesting the relation

$$\xi = \gamma/d_\gamma. \quad (28)$$

On the other hand, under a coordinate transformation $x \mapsto x' = Cx$ one should transform $\phi(x) \mapsto \phi'(x') = \phi(x) - Q \log C$ with $Q = 2/\gamma + \gamma/2$ in order to preserve the γ -Liouville measure (25) [54]. Accordingly, (27) transforms as

$$D'_{\xi,\epsilon}(x', y') = \inf_{\Gamma:x \rightarrow y} \int_0^1 e^{\xi \phi_\epsilon(C\Gamma(t)) - \xi Q \log C} |C\Gamma'(t)| dt \quad (29)$$

$$= C^{1-\xi Q} \inf_{\Gamma:x \rightarrow y} \int_0^1 e^{\xi \phi_{\epsilon/C}(\Gamma(t))} |\Gamma'(t)| dt = C^{1-\xi Q} D_{\xi,\epsilon/C}(x, y). \quad (30)$$

Equality in the limit $\epsilon \rightarrow 0$ can only be achieved if $D_{\xi,\epsilon}(x, y)$ scales as $\epsilon^{1-\xi Q}$ as $\epsilon \rightarrow 0$ (see [25, Section 2.3] for a similar heuristic). Indeed, it was proven rigorously in [25, Theorem 1.5] that the following limit holds (in probability)

$$\frac{\log D_{\xi,\epsilon}(x, y)}{\log \epsilon} \xrightarrow{\epsilon \rightarrow 0} \lambda(\xi), \quad \lambda(\xi) = 1 - \xi Q = 1 - \frac{2}{d_\gamma} - \frac{\gamma^2}{2d_\gamma}. \quad (31)$$

See [27, Theorem 1.1] for results on the limit of $\epsilon^{-\lambda} D_{\xi,\epsilon}(x, y)$ as a metric space.

Note that if we can determine $\lambda(\xi)$ for some value of ξ satisfying $1 - \lambda(\xi) > 2\xi$, then (28) and (31) can be inverted to determine a pair of values γ and d_γ . This provides

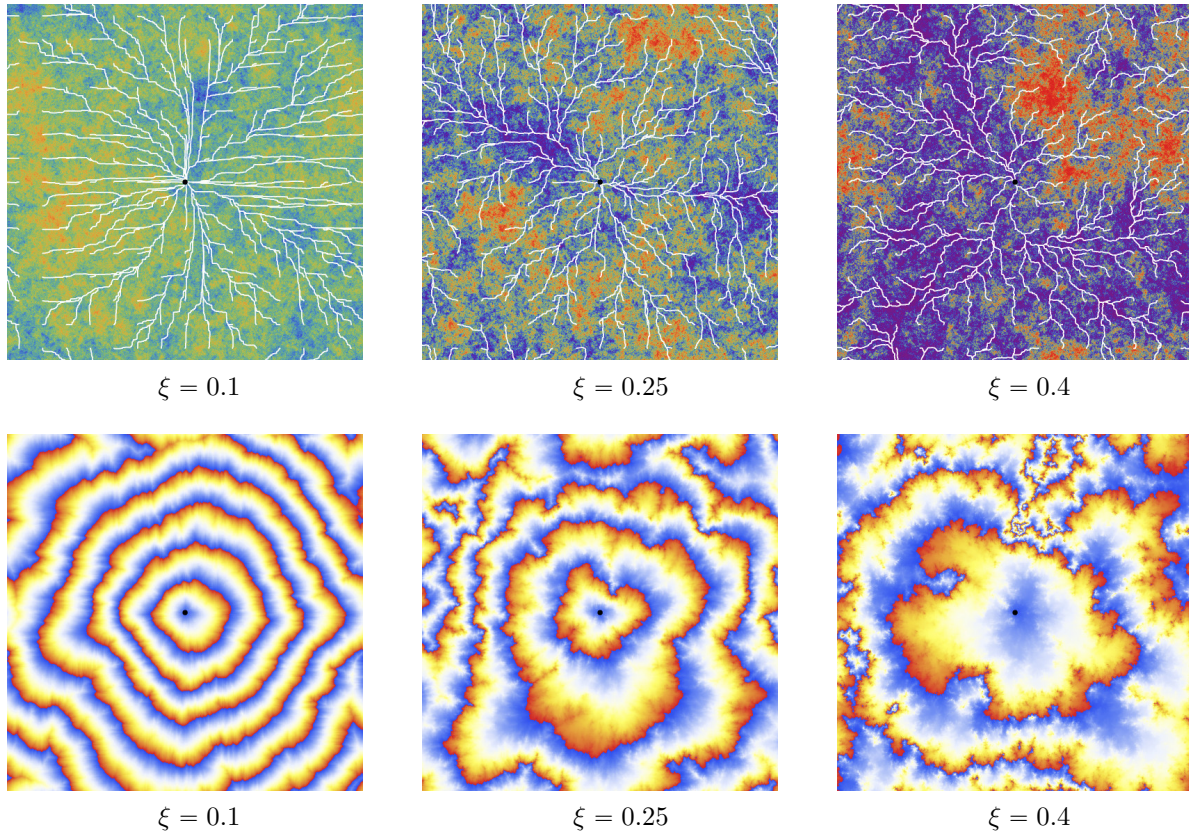


Figure 12: Top: plot of $\xi\psi(x)$ on Λ_{2048} together with the shortest DLFPF paths (white) from 15^2 evenly spaced points to the center of the lattice. Bottom: the DLFPF distance $D_{\xi,w}(x,y)$ from points $x \in \Lambda_{2048}$ to the center y , colored from blue to red according to the fractional part of $\frac{10}{w}D_{\xi,w}(x,y)$. Note: all images use different samples of the discrete Gaussian free field.

a different route towards numerical estimates of d_γ . Watabiki's formula (1) and Ding & Gwynne's formula (5) correspond to the particularly simple relations

$$\lambda^{\text{W}}(\xi) = \xi^2, \quad \lambda^{\text{DG}}(\xi) = \frac{\xi}{\sqrt{6}}. \quad (32)$$

4.3. Discrete Liouville first passage percolation (DLFPF)

The Liouville first passage percolation distance has a natural discrete counterpart [56, 24, 29] that is particularly convenient for numerical simulations. Consider a $w \times w$ square lattice $\Lambda_w := (\mathbb{Z}/w\mathbb{Z})^2$ with periodic boundary conditions. The *discrete Gaussian free field* $\psi : \Lambda_w \rightarrow \mathbb{R}$ on this lattice has probability distribution proportional to

$$\exp\left[-\frac{1}{4\pi} \sum_{x,y \in \Lambda_w} \psi(x) \Delta_{xy} \psi(y)\right] \delta\left(\sum_{x \in \Lambda_w} \psi(x)\right), \quad \Delta_{xy} = \begin{cases} 4 & x = y \\ -1 & x \text{ and } y \text{ adjacent} \\ 0 & \text{otherwise,} \end{cases} \quad (33)$$

which is the natural discrete analogue of $e^{-S_{\text{GFF}}[\phi]}$ in (24). The normalization of the field is such that

$$\langle \psi(0)^2 \rangle \stackrel{w \rightarrow \infty}{\sim} \log w. \quad (34)$$

The natural discretization of the first passage percolation distance is

$$D_{\xi,w}(x, y) = \inf_{\Gamma: x \rightarrow y} \sum_{i=1}^m \frac{1}{2} (e^{\xi\psi(\Gamma(i-1))} + e^{\xi\psi(\Gamma(i))}), \quad (35)$$

where the sum is over nearest-neighbour walks $\Gamma: \{0, 1, \dots, m\} \rightarrow \Lambda_w$ of arbitrary length m from $\Gamma(0) = x$ to $\Gamma(m) = y$. See Figure 12 for a few random samples.

In [29, Theorem 1.4] it is shown, in the slightly different setting of Dirichlet instead of periodic boundary conditions, that this distance approximates the continuum first passage percolation distance (27) well. In particular, it satisfies the analogous scaling relation [29, Theorem 1.5]

$$\frac{\log D_{\xi,w}([wx], [wy])}{\log w} \xrightarrow{w \rightarrow \infty} 1 - \lambda(\xi) \quad (36)$$

for $x, y \in [0, 1]^2$ fixed, where $[wx]$ denotes the lattice point in Λ_w closest to wx .

5. Finite-size scaling of Liouville first passage percolation distance

We make a similar assumption as we did in the case of the random planar maps, namely that the probability density $\rho_{\xi,w}$ of the distance $D_{\xi,w}(x, y)$ between two points x and y sampled uniformly from Λ_w satisfies a pointwise scaling limit

$$\lim_{w \rightarrow \infty} w^{1-\lambda} \rho_{\xi,w}(w^{1-\lambda}r) = \rho_{\xi}(r), \quad r > 0. \quad (37)$$

To estimate $\rho_{\xi,w}$ we have sampled (at least) 2 million instances of the Gaussian free field for w ranging from 2^6 to 2^{12} and ξ from 0.01 to 0.4. For each field we pick an arbitrary starting point x and determine the distances $D_{\xi,w}(x, y)$ to all points $y \in \Lambda_w$, which are then included in a histogram.

As in the case of the planar maps, we fit $x \mapsto k_w^{-1} \rho_{\xi,w}(k_w^{-1}x)$ to the reference distribution $\rho_{\xi,w_0}(x)$, where $w_0 = 2^{12}$ is the largest lattice size considered. As before, only the data for which $\rho_{\xi,w}(r) \geq \nu \max_{r'} \rho_{\xi,w}(r')$ with $\nu = 0.2$ is used in the fit. Figure 13 plots $k_w^{-1} \rho_{\xi,w}(k_w^{-1}x)$ for the fitted values of k_w and various values of ξ . The quality of the collapse is good for the larger values of ξ , and can be further improved by introducing a constant shift as was done before.

For small values of ξ , however, the approach towards the limiting distribution ρ_{ξ} of (37) is markedly slower. In this regime the fitted values of k_w depend more sensitively on the fitting procedure used and one should attribute a larger systematic uncertainty to them. To get a handle on this uncertainty we repeat the analysis with different choices of fitting parameters, namely $\nu = 0, 0.2, \dots, 0.8$ for the range of data used and $s = 0, 2, 4$

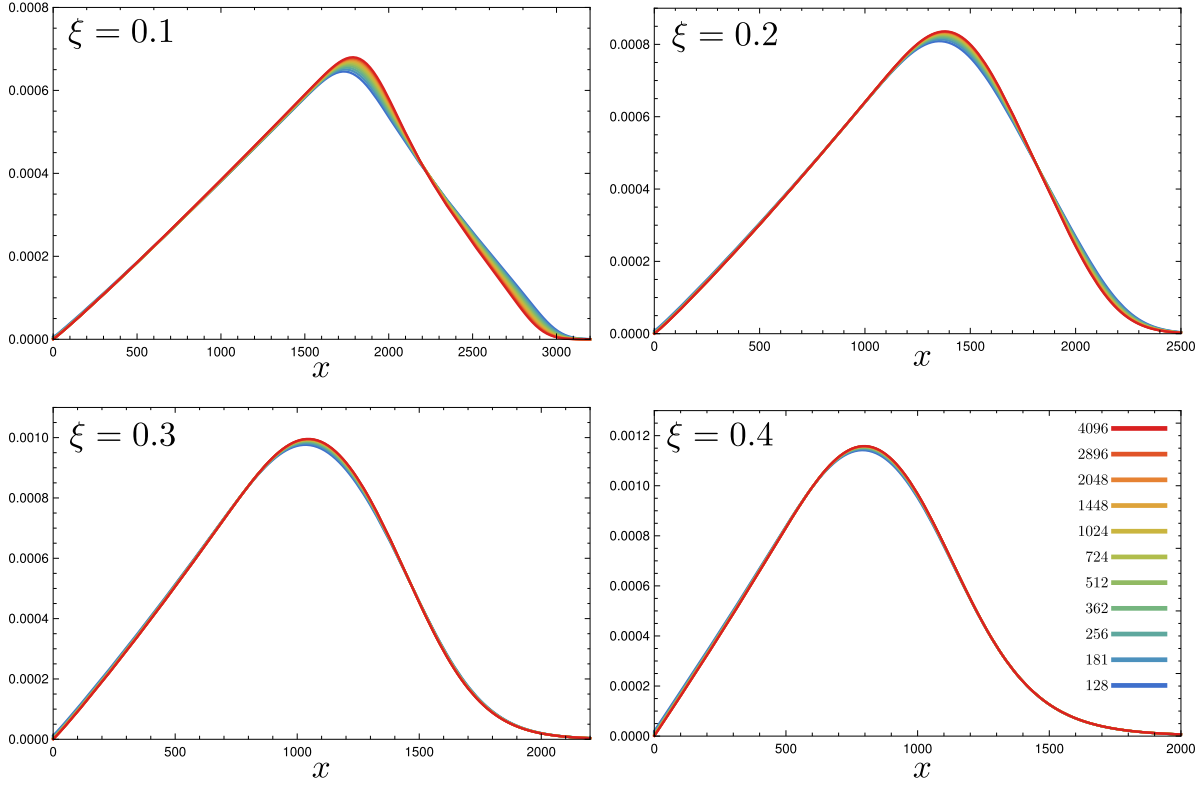


Figure 13: Finite-size scaling of the DLFP distance for $\xi = 0.1, 0.2, 0.3, 0.4$. Shown are plots of $x \mapsto k_w^{-1} \rho_{\xi, w}(k_w^{-1} x)$ with k_w determined by a best fit for $w = 2^7, \dots, 2^{12}$.

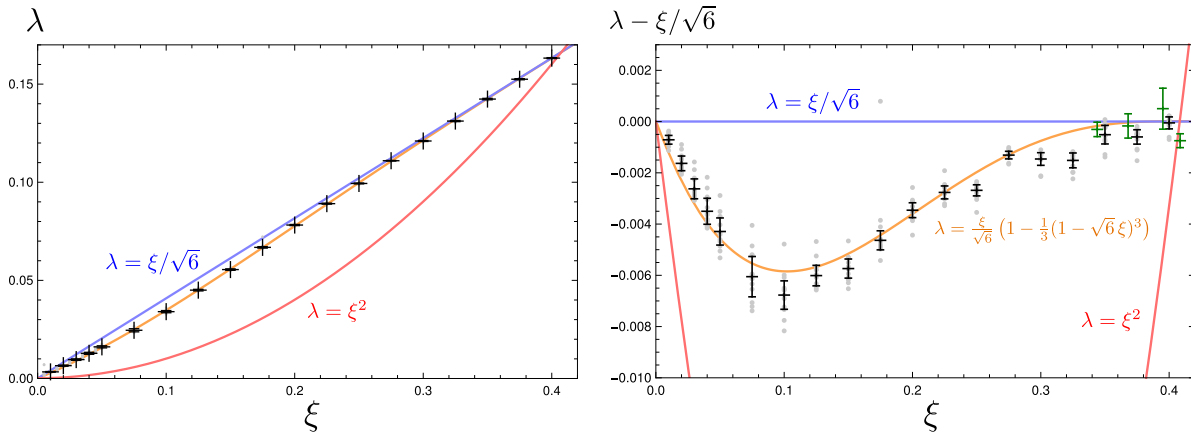


Figure 14: The plot on the left shows the estimates of λ with systematic errors (as recorded in Table 6) in comparison to $\lambda^{\text{W}} = \xi^2$ (red), $\lambda^{\text{DG}} = \xi/\sqrt{6}$ (blue) and $\lambda = \frac{\xi}{\sqrt{6}} \left(1 - \frac{1}{3}(1 - \sqrt{6}\xi)^3\right)$ (orange). The right plot shows the same data normalized by $\xi/\sqrt{6}$, as well as the individual data points for the different parameters ν and s (gray) and the planar map estimates of Table 5 (green).

Table 6: Estimates for λ with systematic errors obtained by fitting to (38).

ξ	λ	c	γ	d_γ
0.010	0.0033 ± 0.0002	-59.6k	0.0201	2.0070 ± 0.0003
0.020	0.0065 ± 0.0003	-14.8k	0.0402	2.0140 ± 0.0006
0.030	0.0096 ± 0.0004	-6.5k	0.0606	2.0213 ± 0.0008
0.040	0.0128 ± 0.0005	-3.6k	0.0812	2.0293 ± 0.0010
0.050	0.0161 ± 0.0005	-2.3k	0.1019	2.0380 ± 0.0011
0.075	0.0246 ± 0.0008	-990.	0.1547	2.0626 ± 0.0017
0.100	0.0341 ± 0.0006	-534.	0.2093	2.0932 ± 0.0012
0.125	0.0450 ± 0.0004	-325.	0.2664	2.1315 ± 0.0009
0.150	0.0555 ± 0.0004	-213.	0.3261	2.1738 ± 0.0009
0.175	0.0668 ± 0.0004	-145.	0.3893	2.2244 ± 0.0010
0.200	0.0782 ± 0.0003	-102.	0.4565	2.2827 ± 0.0008
0.225	0.0891 ± 0.0003	-73.3	0.5285	2.3489 ± 0.0007
0.250	0.0994 ± 0.0002	-52.9	0.6062	2.4247 ± 0.0007
0.275	0.1110 ± 0.0001	-37.7	0.6929	2.5196 ± 0.0005
0.300	0.1210 ± 0.0003	-26.5	0.7888	2.6293 ± 0.0010
0.325	0.1312 ± 0.0003	-17.9	0.8994	2.7675 ± 0.0014
0.350	0.1424 ± 0.0004	-11.0	1.0346	2.9561 ± 0.0022
0.375	0.1525 ± 0.0003	-5.65	1.2076	3.2201 ± 0.0023
0.400	0.1632 ± 0.0002	-1.26	1.4787	3.6968 ± 0.0035

for the constant shift (covering roughly the range of optimal shifts). For each choice of these parameters the values k_w are determined and fitted to the ansatz

$$k_w \approx \left(\frac{w}{w_0}\right)^{\lambda-1} \left(a + b \left(\frac{w}{w_0}\right)^{-\delta}\right) \quad (38)$$

analogous to (22). The collection of values of λ obtained in this way is used to establish the systematic error on our estimate, which turns out to be significantly larger than the statistical error for all $\xi \lesssim 0.35$.

The results are gathered in Table 6, which also includes the corresponding central charge $c = 25 - 6(1 - \lambda)^2/\xi^2$ and estimates for γ and d_γ calculated using (28) and (31). We only record the error in d_γ explicitly, because it is most significant when comparing to the formulas d_γ^{DG} and d_γ^{W} . Figure 14 shows a plot of the estimated values of λ , while Figure 15 displays the corresponding estimates for the Hausdorff dimension d_γ .

6. Discussion

The DLFPP estimates of λ and d_γ for $\xi = 0.35, 0.375, 0.4$ are in very good agreement with Ding & Gwynne's prediction $\lambda^{\text{DG}} = \xi/\sqrt{6}$ and consistent with the random planar map results (see the green data points in Figure 14 and Figure 15). For $\xi < 0.35$ the measurements are still much closer to λ^{DG} than to Watabiki's prediction $\lambda^{\text{W}} = \xi^2$, but a significant negative deviation is visible, that is most pronounced at around $\xi = 0.1$ ($\gamma \approx 0.2$, $c \approx -2.3k$). The data is better described by the (completely ad hoc) formula

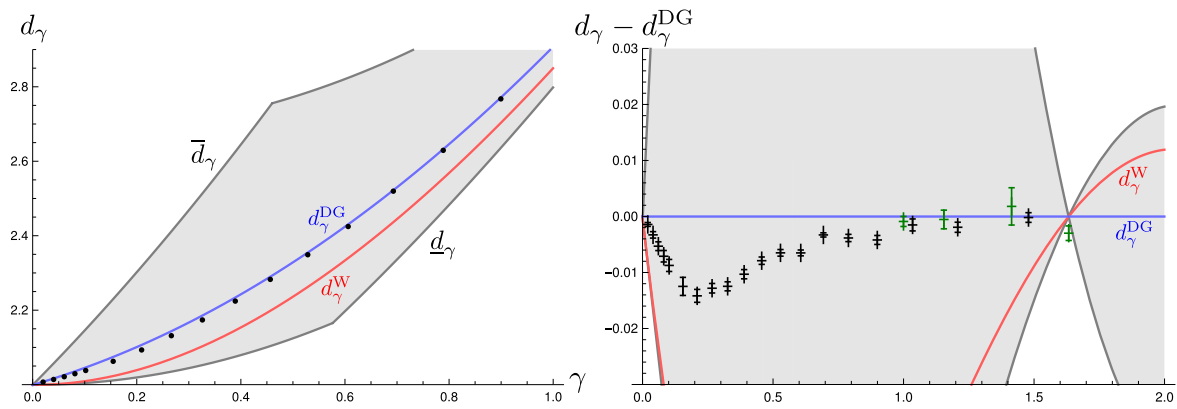


Figure 15: Left: The DLFPF estimates of d_γ (error bars too small to display). Right: the estimates of d_γ normalized by d_γ^{DG} with error bars as obtained from DLFPF (black) and random planar maps (green).

$\lambda = \frac{\xi}{\sqrt{6}} \left(1 - \frac{1}{3}(1 - \sqrt{6}\xi)^3\right)$. However, we are hesitant to rule out $\lambda^{\text{DG}} = \xi/\sqrt{6}$ on the basis of the current data. The reason for this is that the quality of the finite-size scaling for smaller values of ξ is not as good as one may have hoped, indicating that (much) larger lattice sizes might be necessary to observe accurate scaling. An explanation could be that for small ξ and currently used lattice sizes, the DLFPF geodesics are too close to geodesics of the Euclidean lattice and therefore do not sufficiently display their fractal structure. Indeed, in Figure 12 many of the DLFPF geodesics for $\xi = 0.1$ are seen to contain fairly long straight segments, a phenomenon that becomes more pronounced for even smaller ξ . Since the DLFPF length of straight segments scales with an exponent that is different but for small ξ quite close to $1 - \lambda$, one may need to increase the lattice size w considerably to make its subleading contribution small enough.

Source code and simulation data

The source code and simulation data, on which Section 3 and Section 5 are based, are freely available online at [57].

References

- [1] Ambjørn J, Jurkiewicz J and Loll R 2005 The spectral dimension of the universe is scale dependent *Physical review letters* **95** 171301
- [2] Benedetti D 2009 Fractal properties of quantum spacetime *Physical review letters* **102** 111303
- [3] Reuter M and Saueressig F 2011 Fractal space-times under the microscope: a renormalization group view on monte carlo data *Journal of High Energy Physics* **2011** 12
- [4] Calcagni G, Oriti D and Thürigen J 2015 Dimensional flow in discrete quantum geometries *Physical Review D* **91** 084047
- [5] Carlip S 2017 Dimension and dimensional reduction in quantum gravity *Classical and Quantum Gravity* **34** 193001
- [6] Knizhnik V G, Polyakov A M and Zamolodchikov A B 1988 Fractal structure of 2d-quantum gravity *Modern Physics Letters A* **3** 819–826

- [7] Ambjørn J and Watabiki Y 1995 Scaling in quantum gravity *Nuclear Physics B* **445** 129–142
- [8] Chassaing P and Schaeffer G 2004 Random planar lattices and integrated superBrownian excursion *Probab. Theory Related Fields* **128** 161–212
- [9] Angel O 2003 Growth and percolation on the uniform infinite planar triangulation *Geom. Funct. Anal.* **13** 935–974
- [10] Le Gall J F 2013 Uniqueness and universality of the Brownian map *Ann. Probab.* **41** 2880–2960
- [11] Miermont G 2013 The Brownian map is the scaling limit of uniform random plane quadrangulations *Acta Math.* **210** 319–401
- [12] Miller J and Sheffield S 2016 Liouville quantum gravity and the Brownian map II: geodesics and continuity of the embedding (*Preprint arXiv:1605.03563*)
- [13] Ambjørn J, Nielsen J L, Rolf J, Boulatov D and Watabiki Y 1998 The spectral dimension of 2D quantum gravity *Journal of High Energy Physics* **1998** 010
- [14] Rhodes R and Vargas V 2014 Spectral dimension of Liouville quantum gravity *Annales Henri Poincaré* vol 15 (Springer) pp 2281–2298
- [15] Gwynne E and Miller J 2017 Random walk on random planar maps: spectral dimension, resistance, and displacement (*Preprint arXiv:1711.00836*)
- [16] Watabiki Y 1993 Analytic study of fractal structure of quantized surface in two-dimensional quantum gravity *Progress of Theoretical Physics Supplement* **114** 1–17
- [17] Ambjørn J, Jurkiewicz J and Watabiki Y 1995 On the fractal structure of two-dimensional quantum gravity *Nuclear Physics B* **454** 313–342
- [18] Kawamoto N, Kazakov V, Saeki Y and Watabiki Y 1992 Fractal structure of two-dimensional gravity coupled to $c = -2$ matter *Physical review letters* **68** 2113
- [19] Anagnostopoulos K, Bialas P and Thorleifsson G 1999 The ising model on a quenched ensemble of $c = -5$ gravity graphs *Journal of statistical physics* **94** 321–345
- [20] Kawamoto N and Yotsuji K 2002 Numerical study for the c -dependence of fractal dimension in two-dimensional quantum gravity *Nuclear Physics B* **644** 533–567
- [21] Ambjørn J and Budd T G 2012 Semi-classical dynamical triangulations *Physics Letters B* **718** 200–204
- [22] Ambjørn J and Budd T 2013 The toroidal Hausdorff dimension of 2d Euclidean quantum gravity *Physics Letters B* **724** 328–332
- [23] Ambjørn J and Budd T 2014 Geodesic distances in Liouville quantum gravity *Nuclear Physics B* **889** 676 – 691
- [24] Ding J and Goswami S 2018 Upper bounds on Liouville first-passage percolation and Watabiki’s prediction *Commun. on Pure and Applied Mathematics* (*Preprint arXiv:1610.09998*)
- [25] Ding J and Gwynne E 2018 The fractal dimension of Liouville quantum gravity: universality, monotonicity, and bounds *Commun. Math. Phys.* 1–58 (*Preprint arXiv:1807.01072*)
- [26] Dubédat J, Falconet H, Gwynne E, Pfeffer J and Sun X 2019 Weak LQG metrics and Liouville first passage percolation (*Preprint arXiv:1905.00380*)
- [27] Gwynne E and Miller J 2019 Existence and uniqueness of the Liouville quantum gravity metric for $\gamma \in (0, 2)$ (*Preprint arXiv:1905.00383*)
- [28] Gwynne E and Pfeffer J 2019 Bounds for distances and geodesic dimension in Liouville first passage percolation (*Preprint arXiv:1903.09561*)
- [29] Ang M 2019 Comparison of discrete and continuum Liouville first passage percolation (*Preprint arXiv:1904.09285*)
- [30] Kenyon R, Miller J, Sheffield S and Wilson D B 2015 Bipolar orientations on planar maps and SLE_{12} (*Preprint arXiv:1511.04068*)
- [31] Gwynne E and Pfeffer J 2019 External diffusion limited aggregation on a spanning-tree-weighted random planar map (*Preprint arXiv:1901.06860*)
- [32] Li Y, Sun X and Watson S S 2017 Schnyder woods, SLE_{16} , and Liouville quantum gravity (*Preprint arXiv:1705.03573*)
- [33] Tutte W T 1963 A census of planar maps *Canadian J. Math.* **15** 249–271

- [34] Schaeffer G 1998 *Conjugation d'arbres et cartes combinatoires aleatoires* Ph.D. thesis Universit Bordeaux I
- [35] Miermont 2014 *Aspects of Random Maps* (Saint-Flour lecture notes)
- [36] Mullin R C 1967 On the enumeration of tree-rooted maps *Canadian J. Math.* **19** 174–183
- [37] Sheffield S 2016 Quantum gravity and inventory accumulation *Ann. Probab.* **44** 3804–3848
- [38] Tutte W T 1973 Chromatic sums for rooted planar triangulations: the cases $\lambda = 1$ and $\lambda = 2$ *Canadian J. Math.* **25** 426–447
- [39] Bousquet-Mélou M 2011 Counting planar maps, coloured or uncoloured *Surveys in combinatorics 2011 (London Math. Soc. Lecture Note Ser. vol 392)* (Cambridge Univ. Press, Cambridge) pp 1–49
- [40] Gwynne E, Holden N and Sun X 2016 Joint scaling limit of a bipolar-oriented triangulation and its dual in the peanosphere sense (*Preprint arXiv:1603.01194*)
- [41] Bousquet-Mélou M, Fusy É and Raschel K 2019 Plane bipolar orientations and quadrant walks (*Preprint arXiv:1905.04256*)
- [42] Bousquet-Mélou M and Mishna M 2010 Walks with small steps in the quarter plane *Algorithmic probability and combinatorics (Contemp. Math. vol 520)* (Amer. Math. Soc., Providence, RI) pp 1–39
- [43] Schnyder W 1989 Planar graphs and poset dimension *Order* **5** 323–343
- [44] Bonichon N 2005 A bijection between realizers of maximal plane graphs and pairs of non-crossing Dyck paths *Discrete Math.* **298** 104–114
- [45] Bernardi O and Bonichon N 2009 Intervals in Catalan lattices and realizers of triangulations *J. Combin. Theory Ser. A* **116** 55–75
- [46] Fusy E, Poulalhon D and Schaeffer G 2009 Bijective counting of plane bipolar orientations and Schnyder woods *European J. Combin.* **30** 1646–1658
- [47] Bouttier J, Di Francesco P and Guitter E 2003 Geodesic distance in planar graphs *Nuclear Physics B* **663** 535–567
- [48] Ferrenberg A M and Landau D 1991 Critical behavior of the three-dimensional Ising model: A high-resolution Monte Carlo study *Physical Review B* **44** 5081
- [49] Ambjørn J, Anagnostopoulos K, Ichihara T, Jensen L, Kawamoto N, Watabiki Y and Yotsuji K 1998 The Quantum space-time of $c = -2$ gravity *Nucl. Phys.* **B511** 673–710 (*Preprint hep-lat/9706009*)
- [50] Gwynne E, Miller J and Sheffield S 2017 The Tutte embedding of the mated-CRT map converges to Liouville quantum gravity (*Preprint arXiv:1705.11161*)
- [51] David F 1988 Conformal field theories coupled to 2-d gravity in the conformal gauge *Modern Physics Letters A* **3** 1651–1656
- [52] Distler J and Kawai H 1989 Conformal field theory and 2d quantum gravity *Nuclear physics B* **321** 509–527
- [53] Sheffield S 2007 Gaussian free fields for mathematicians *Probab. Theory Relat. Fields* **139** 521–541
- [54] Duplantier B and Sheffield S 2011 Liouville quantum gravity and KPZ *Invent. Math.* **185** 333–393
- [55] Ding J, Zeitouni O and Zhang F 2019 Heat kernel for Liouville Brownian motion and Liouville graph distance *Communications in Mathematical Physics* (*Preprint arXiv:1807.00422*)
- [56] Benjamini I 2010 Random planar metrics *Proceedings of the International Congress of Mathematicians* vol 4 (World Scientific Publishing Company) pp 2177–2187
- [57] Barkley J and Budd T 2019 Simulation data and source code for Hausdorff dimension measurements in two-dimensional quantum gravity *Zenodo* doi:10.5281/zenodo.3375454